

Article

# Hydroxyapatite Biosynthesis Obtained from Sea Urchin Spines (*Strongylocentrotus purpuratus*): Effect of Synthesis Temperature

Nayeli Sarahi Gómez Vázquez<sup>1</sup>, Priscy Alfredo Luque Morales<sup>1,\*</sup>, Claudia Mariana Gomez Gutierrez<sup>1</sup>, Osvaldo de Jesus Nava Olivas<sup>1</sup>, Ruben Cesar Villarreal Sánchez<sup>1</sup>, Alfredo Rafael Vilchis Nestor<sup>2</sup> and Manuel de Jesús Chinchillas Chinchillas<sup>1,\*</sup>

<sup>1</sup> Facultad de Ingeniería, Arquitectura y Diseño-Universidad Autónoma de Baja California, 22860 Ensenada, B.C., Mexico; ngomez70@uabc.edu.mx (N.S.G.V.); cmgomezg@uabc.edu.mx (C.M.G.G.); navao@uabc.edu.mx (O.d.J.N.O.); ruben.villarreal@uabc.edu.mx (R.C.V.S.)

<sup>2</sup> Centro Conjunto de Investigación en Química Sustentable, UAEM-UNAM, 50200 Toluca, Mexico; arvilchisn@uaemex.mx

\* Correspondence: pluque@uabc.edu.mx (P.A.L.M.); manuel.chinchillas@uabc.edu.mx (M.d.J.C.C.); Tel.: +52-1-646-132-0838 (P.A.L.M.); +52-1-668-397-8139 (M.d.J.C.C.)

Received: 20 February 2020; Accepted: 9 April 2020; Published: 22 April 2020



**Abstract:** In this investigation, hydroxyapatite (HA) was synthesized using sea urchin spines (*Strongylocentrotus purpuratus*) via a precipitation and heat treatment method at three different temperatures (500, 600 and 700 °C). Biosynthesized HA was characterized to determine the vibration of functional groups, morphology, particle size, crystalline structure and chemical composition. For this, Fourier-Transform Infrared Spectroscopy with Attenuated Total Reflectance (FTIR-ATR), Scanning Electron Microscopy (SEM) coupled with Energy Dispersive X-ray Spectroscopy (EDS), X-ray Diffraction (XRD) and X-ray Photoelectron Spectroscopy (XPS) were used, respectively. The FTIR-ATR results reveal that the most defined characteristic HA bonds (O-H, P-O and C-O bonds) were better defined at higher synthesis temperatures. SEM also presented evidence that temperature has a significant effect on morphology. EDS results showed that the Ca/P ratio increased in the samples at higher temperatures. XRD analysis presented the characteristic peaks of HA, showing a lower crystallinity when the synthesis temperature increased. Finally, the XPS confirmed that the material resulting from biosynthesis was HA. Hence, according to these results, the synthesis temperature of HA has a significant effect on the characteristics of the resulting material.

**Keywords:** biomaterial; hydroxyapatite; sea urchin; *Strongylocentrotus purpuratus*

## 1. Introduction

Hydroxyapatite (HA), an important crystalline material in the medical field, is composed of calcium, phosphorus and hydrogen atoms ( $\text{Ca}_{10}(\text{PO}_4)_6(\text{HO})_2$ ) and generally has a hexagonal crystalline structure [1]. This material is present in teeth and bones, presenting a characteristic hardness and, due to its chemical and physical properties, has the application of facilitating the regeneration of hard tissues [2]. It is identified as a non-toxic material, with high biocompatibility, bioactivity and similarity with the chemical composition of the inorganic part of bone tissue [3,4]. It is the component with the highest percentage in bones [5], which are composed of approximately 70% inorganic HA [6]. HA has been used in sensors in liquid and gaseous environments [7], in the treatment of wastewater to adsorb dyes [8] and as a coating on metallic body implants [9], among other uses. This last application stems from the need to repair large bone defects and avoid the use of autografts and allografts, which often involve limitations such as rejection rate, insufficient donors or a high risk of disease transmission [10].

The investigation of new substitutes for bone reconstruction is necessary in order to meet existing medical standards and needs [11].

The investigation of new generation methods, from biosynthesis or biogenic sources, has provided the advantages of reducing both production costs and toxicity, as naturally found materials are used which exhibit better bone conductivity compared to methods that involve common inorganic sources [12]. In 2018, Ofudje et al. synthesized HA by thermal decomposition from pig bones, generating crystal sizes from 11 to 21 nm [13]. Rahavi et al. (2017) generated nanometric HA (20–100 nm approximately) by calcinating human, bovine, camel and horse bones at 700 °C, while also using the sol–gel method [14]. Alternatively, in the work of Shi et al. in 2018, HA with a size of 100, 200 and 250 nm was synthesized from trout, salmon and cod bones, respectively [15]. It is also possible to obtain HA by mechanical-chemical synthesis from eggshells, as described by Ferro and Guedes in 2019, achieving crystal sizes ranging from 20 to 40 nm [16]. It is also possible to use marine debris for HA production. Edgar Mancilla et al. (2019) managed to synthesize HA from sea urchin spine debris [17]. Marine debris has caused severe pollution problems in ecosystems and problems in the reproduction of other species. At present, marine debris has not been widely used for the synthesis of HA [18]. The fishing of many marine species generates a great deal of sea pollution. Within these species is the sea urchin (*Strongylocentrotus purpuratus*), an invertebrate animal that has been recognized as a key species to boost community-level dynamics by grazing seaweed and creating moors [19]. The cultivation of this marine species generates a high monetary value and a high demand in the international market. The commercial exploitation of sea urchin in Mexico began in Baja California in 1993, and it has become more important due to the reduction of intense sea urchin fishing since 2001 [20]. The world production of sea urchins was around 117,000 tons per year in 1998, with the United States, Chile and Japan being the largest producers. Japan and France were the main consumers. However, its production has been decreasing significantly since 2009, when it was recorded that sea urchin production decreased by 38% [21]. Adding to this, the extraction of sea urchin aims to take advantage of only its gonads [22], the rest of the urchin (intestines, esophagus, shell and spines) is discarded in landfills, causing bad odors during transportation and decomposition. When the concentration of waste increases, it generates environmental pollution which becomes critical for humans, animals and vegetation near the vicinity [23]. This is why it has become essential to investigate appropriate sea urchin waste recycling methods. In this research, HA was generated from sea urchin spines at relatively high temperatures, causing considerable energy costs. By recycling a waste material to make another material that can be used in various applications, it creates a sustainable process which, with the necessary research, could be generated on an industrial scale. For these reasons, this investigation is a continuation of the aforementioned work [17], and is centered on recycling sea urchin spines by giving them a chemical treatment to produce HA and evaluating the effect of different temperatures on the properties of the synthesized HA crystals.

## 2. Materials and Methods

### 2.1. Materials

For the development of this work, we used sea urchin spines (*Strongylocentrotus purpuratus*) as a precursor to  $\text{Ca}(\text{OH})_2$ , obtained directly from the region of Baja California, Mexico; 85%  $\text{H}_3\text{PO}_4$ , acquired from Sigma Aldrich (St. Louis, MO, USA); and distilled water, used as a means of hydration.

### 2.2. Sea Urchin Spines

The sea urchin spines were collected at a landfill in Baja California and subsequently washed with water to remove contaminants. Finally, the sea urchin spines were trimmed to approximately 10 mm in size.

### 2.3. CaO Synthesis

For the CaO synthesis, the sea urchin spines were washed with distilled water until the organic soft matter present was eliminated. They were then dried in an oven for 30 min at 100 °C. They were subsequently weighed and ground until a fine powder was obtained. Finally, the powder was placed in an oven for 10 min at 800 °C, with an initial 12 °C/min heat ramp.

### 2.4. Ca(OH)<sub>2</sub> Synthesis

After obtaining the CaO, 145 mg was placed in a beaker with 5 mL of distilled water and stirred for 15 min at 35 °C.

### 2.5. HA Synthesis

For the HA synthesis, after the 15 min of stirring in the previous Ca(OH)<sub>2</sub> synthesis, 70 µL of H<sub>3</sub>PO<sub>4</sub> was added at a rate of 1 drop/second to the continuously stirring beaker. Once the H<sub>3</sub>PO<sub>4</sub> was added, stirring continued for 18 h at the same temperature (35 °C). The product was then filtered and washed with distilled water until a neutral pH was obtained. The material was then dried at 60 °C on a magnetic stirrer and finally given a 500 °C heat treatment in an oven at a 12 °C/min heat ramp. Two other samples were prepared varying only in the heat treatment temperatures of 600 and 700 °C. The samples were identified as “HA500”, “HA600” and “HA700”, with the numbers indicating the synthesis temperature. The procedure described in the methodology can be seen in Figure 1.

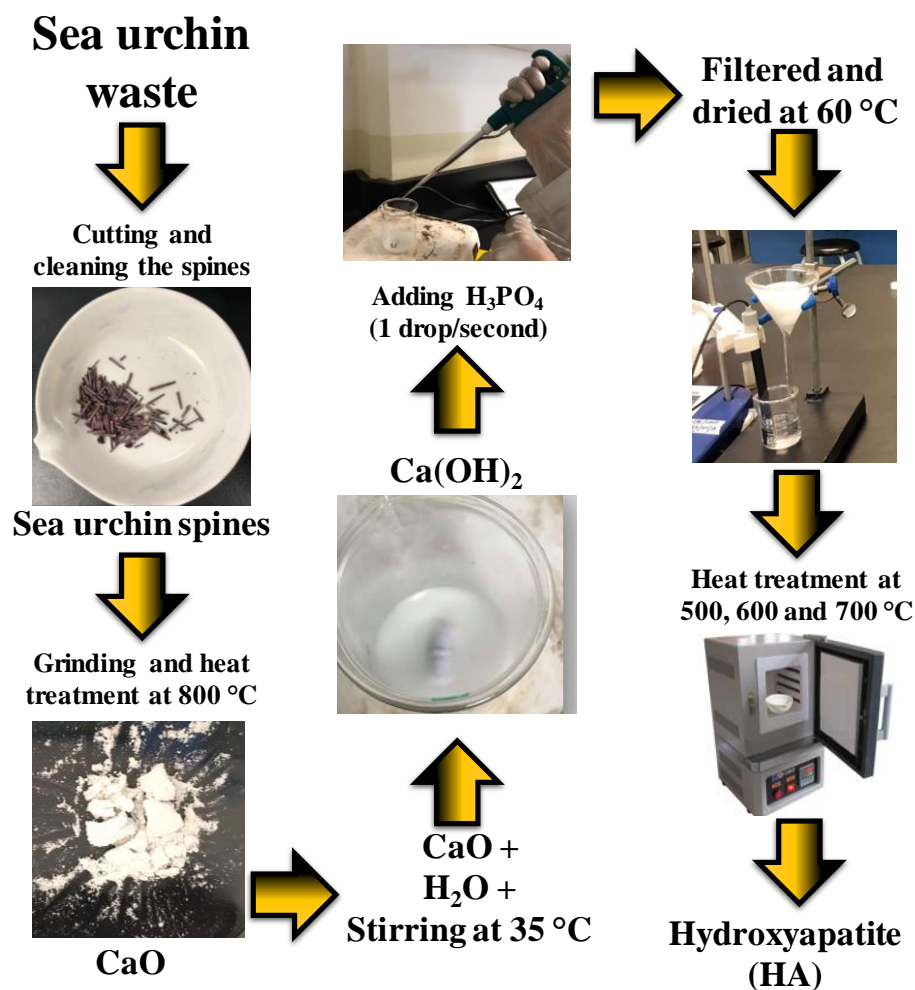


Figure 1. Biosynthesized hydroxyapatite (HA) from sea urchin spines.

## 2.6. Characterization

The HA bond vibrations were analyzed via FTIR-ATR (Perkin Elmer, Waltham, MA, USA) in a PerkinElmer brand device, with a direct transmittance detector and a resolution of  $0.5\text{ cm}^{-1}$ . The morphology and elemental composition were analyzed by means of a JEOL brand SEM-EDS (JEOL, Akishima, Tokyo, Japan), model JSM-6490LV, with a working distance of 11 mm and a voltage of 20 kV. The XRD analysis (Bruker, Billerica, MA, USA) was carried out using a Bruker D2 Phaser brand device, at 30 kV, 10 mA, and in a  $2\theta$  range of  $10\text{--}80^\circ$ . Lastly, the chemical composition XPS was carried out in a Kratos Axis Ultra (Trafford Park, Manchester, UK), with an X-ray irradiation source of aluminum ( $\text{Al}\alpha$ ) and a pressure of  $8 \times 10^{-9}$  Torr.

## 3. Results and Discussion

### 3.1. FTIR-ATR

As seen in Figure 2, the band shown around  $562\text{ cm}^{-1}$  is attributed to the flex mode of phosphate ( $\text{PO}_4^{3-}$ ) bonds [24]. The band at  $600\text{ cm}^{-1}$  belongs to the flex modes of the hydroxyl group in HA [25]. The band at  $873\text{ cm}^{-1}$  corresponds to the Ca–O bond [26,27], which could appear as a result of a small amount of  $\text{CaCO}_3$  present in the samples [28], or due to the decomposition of HA due to dehydration, as reported by Shih in 2018 [15]. In addition to these vibrations, the vibrational band corresponding to the asymmetric stretching mode of phosphate ( $\text{PO}_4^{3-}$ ) is shown at  $1030\text{ cm}^{-1}$ , indicating the formation of HA [29]. Lastly, the signals represented at 960 and  $1410\text{ cm}^{-1}$  indicate the presence of the residual ( $\text{CO}_3^{2-}$ ) carbonate groups. These bands correspond to the  $\nu_2$  vibration mode [30], which arises due to the absorption of carbon dioxide from the surrounding atmosphere during synthesis. However, carbonate-containing HA is chemically similar to the biological apatite found in bones, and is reported to have high bioactivity [31]. Furthermore, there are no vibrations of the organic contamination bonds observed in the FTIR-ATR spectrum, so these results indicate high-purity HA. Here we observed the very important role temperature plays in the formation of HA. It can be seen that a phase change occurred in the sample of biosynthesized HA at  $700\text{ }^\circ\text{C}$ , which has previously been reported in the literature for HA calcined over  $650\text{ }^\circ\text{C}$  and attributed to the transformation of apatite into tricalcium phosphate. As the temperature increased, so did the intensity of the carbonate bonds ( $\text{CO}_3^{2-}$ ) at  $960\text{ cm}^{-1}$ , and the appearance of the vibration at  $1410\text{ cm}^{-1}$ , in addition to a greater intensity of the vibration of the bonds of phosphate ( $\text{PO}_4^{3-}$ ) at  $1030$  and  $562\text{ cm}^{-1}$  [32,33].

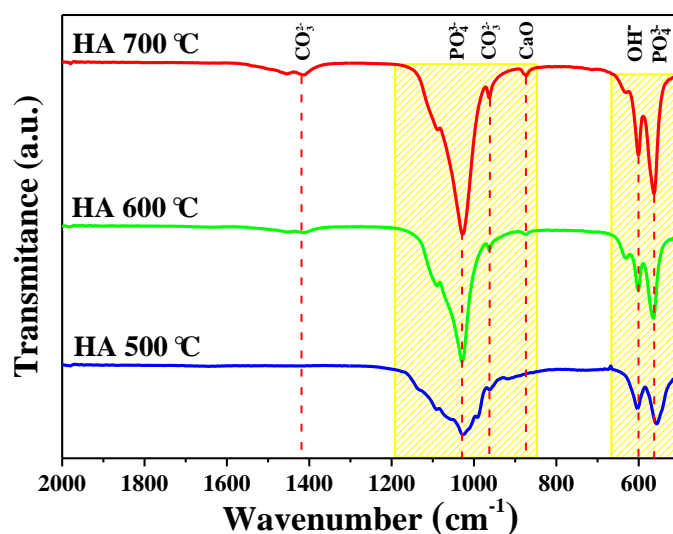
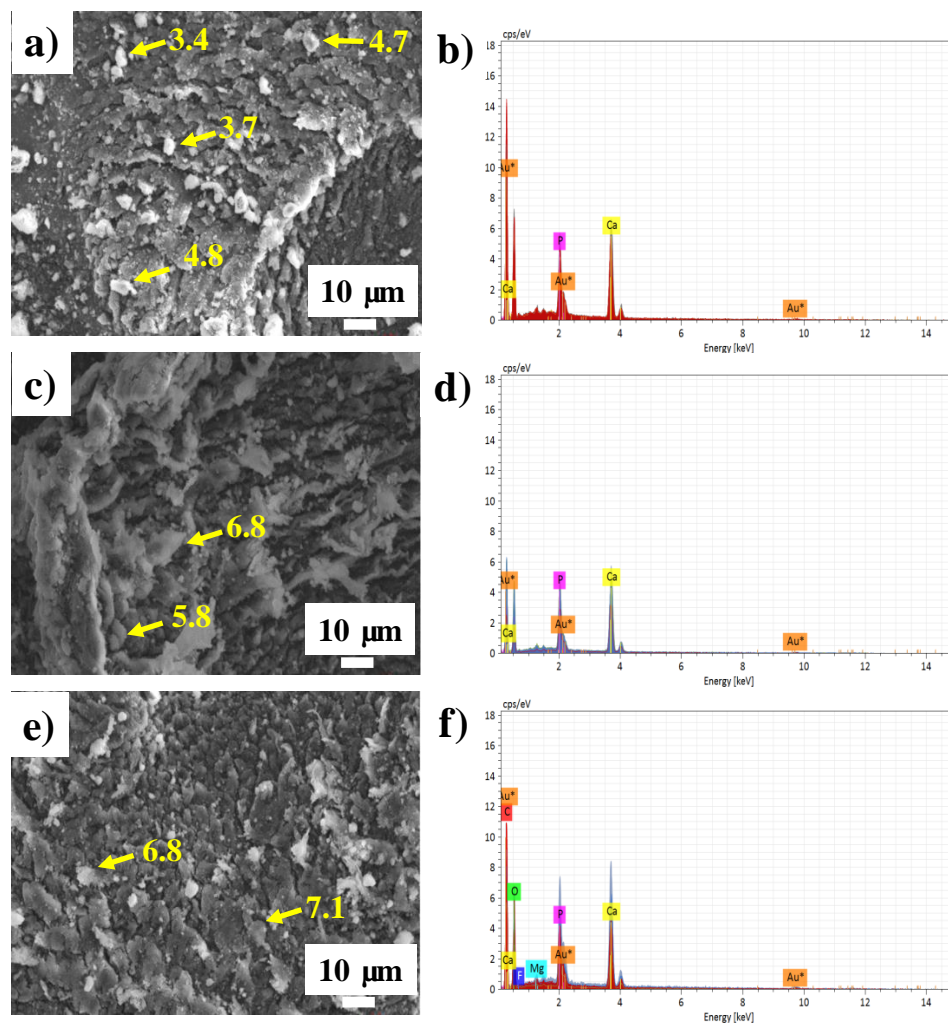


Figure 2. FTIR-ATR spectrum of the three HA samples synthesized at different temperatures.

### 3.2. SEM-EDS

The SEM analysis of the microstructure, as well as the elemental chemical composition (EDS) spectra of the HA samples, are shown in Figure 3. The micrographs of the three analyzed samples (HA700, HA600 and HA500) show a typical HA morphology in the shape of scales [34]. The morphology of the HA synthesized at 700 °C (HA700) is observed in Figure 3a, which shows some HA crystals with varying sizes (between 3.4 and 4.8  $\mu\text{m}$ ) being suspended on an agglomeration of material. The EDS analysis of this micrograph (Figure 3b) shows that the elements of HA (Ca and P) were effectively present. In contrast, the HA sample synthesized at 600 °C presented a slight change in the morphology of the material. The HA synthesized at this temperature did not have a defined shape (Figure 3c) and the size varied between 5.8 and 7  $\mu\text{m}$ . The EDS analysis also shows the elements of Ca and P in the HA600 sample (Figure 3d). Finally, the HA samples synthesized at 500 °C showed a morphology similar to the synthesis of HA at 700 °C, where material is suspended on an agglomeration in the form of scales, as seen in Figure 3e. The approximate size of the crystals was from 6.8 to 7.1  $\mu\text{m}$ . The presence of the Au peak, which corresponds to the coating of gold the samples undergo for analysis, can also be observed in all three samples. The effect of temperature plays a very important role in the characteristics of synthesized HA, since the HA700 sample could be the one with the strongest structure.



**Figure 3.** Elemental morphology and composition for HA samples: (a,b) SEM HA700; (c,d) SEM HA600; (e,f) SEM HA500.

### 3.3. XRD

The X-ray diffraction spectra of all the samples analyzed, which are shown in Figure 4, were compared with the data on the ICDD 9-432 card of the International Center for Diffraction Data, which corresponds to a pure phase of HA [35–37]. The peaks shown at  $26^\circ$ ,  $32^\circ$ ,  $40.1^\circ$ ,  $47^\circ$ ,  $49.5^\circ$  and  $53.6^\circ$  in  $2\theta$  correspond to the crystalline planes (002), (211), (310), (203), (213) and (004), respectively. Here, what stands out is that the crystalline planes (210) and (212) appear at a higher synthesis temperature, specifically in the HA700 sample, and are not present in the other samples. These correspond to the CaO present in the material after the HA dehydroxylation at  $2\theta$  of  $29.1^\circ$  and  $37.4^\circ$  [38]. Alternatively, it was observed that the intensity of some peaks decreases and they become wider as the temperature increases. This indicates that the crystallinity of HA was lower at higher synthesis temperatures. The decrease in the crystallinity of the HA700 sample is due to the phase transformation that the apatite underwent into tricalcium phosphate, which has been reported to contain a semicrystalline structure [32]. The crystal size was also determined using both the Scherrer equation and the diffractogram of each material. Using these methods, sizes from 4.2 to 4.6 nm were observed. The sample that presented a smaller size was HA700, and the largest was HA500. The difference in synthesis temperature had an influence on the size of the crystals. The higher the temperature was, the smaller the size; conversely, the crystallite size was larger at a lower temperature [39]. The causes for this are the increase in solubility, the disaggregation of the phases and the increase in the reaction kinetics during HA formation [40,41].

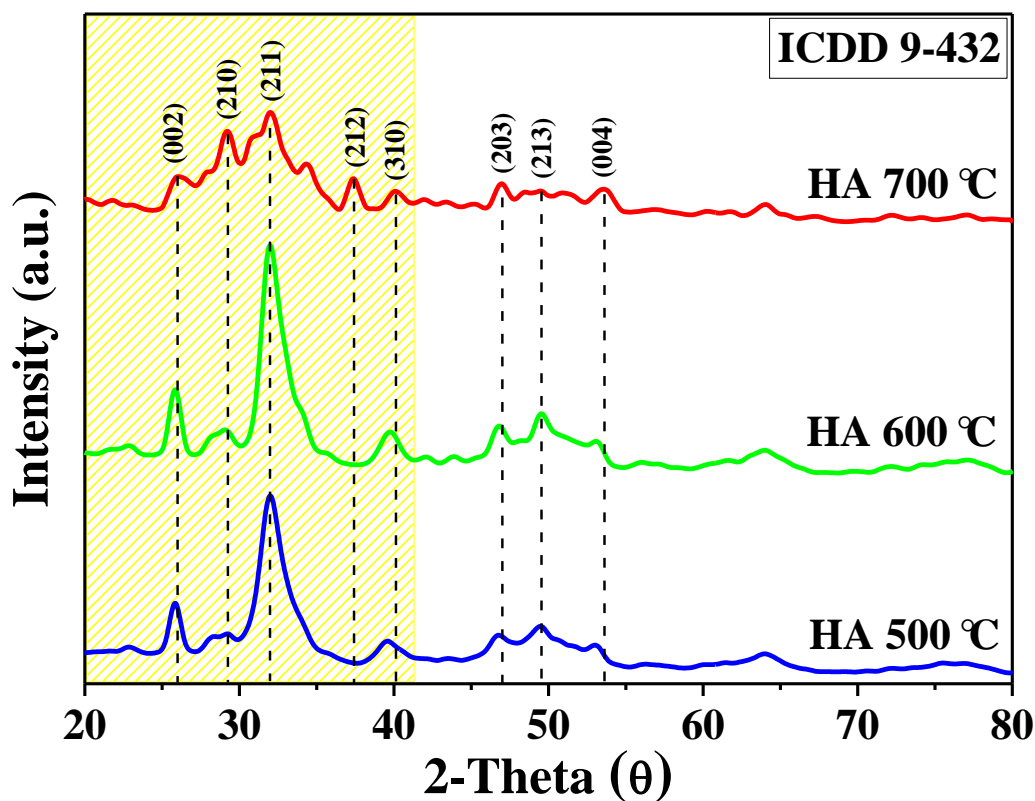


Figure 4. XRD spectra of the three HA samples synthesized at different temperatures.

### 3.4. XPS

XPS was used to study the chemical composition of the synthesized HA. The general spectrum is observed in Figure 5a in which the peaks of O, Ca, C and P can be observed. The energy of the main peak was taken as a reference (C 1s at 284.5 eV). The peaks were observed at 977.5, 530.5, 438.5, 347.5, 284.5, 133.5 and 23.5 eV, corresponding to O Auger KLL, O 1s, Ca 2s, Ca  $2p^{1/2}$ , C 1s, P 2p and

Ca 3p, respectively [42]. In addition, the high-resolution spectra of Ca 2p and O 1s can be observed in Figure 5b,c, respectively, with which the specific energies of 347.5 and 350.9 eV for Ca 2p<sup>3/2</sup> and Ca 2p<sup>1/2</sup> could respectively be obtained. These are in a 2:1 ratio with an energy difference of 3.4 eV, and are typical values for HA [43]. In contrast, the XPS spectrum of O 1s, at the core level, shows a peak at 533.5 eV, which is assigned to the phosphate group [44]. This study demonstrates a successful HA synthesis starting from sea urchin spines.

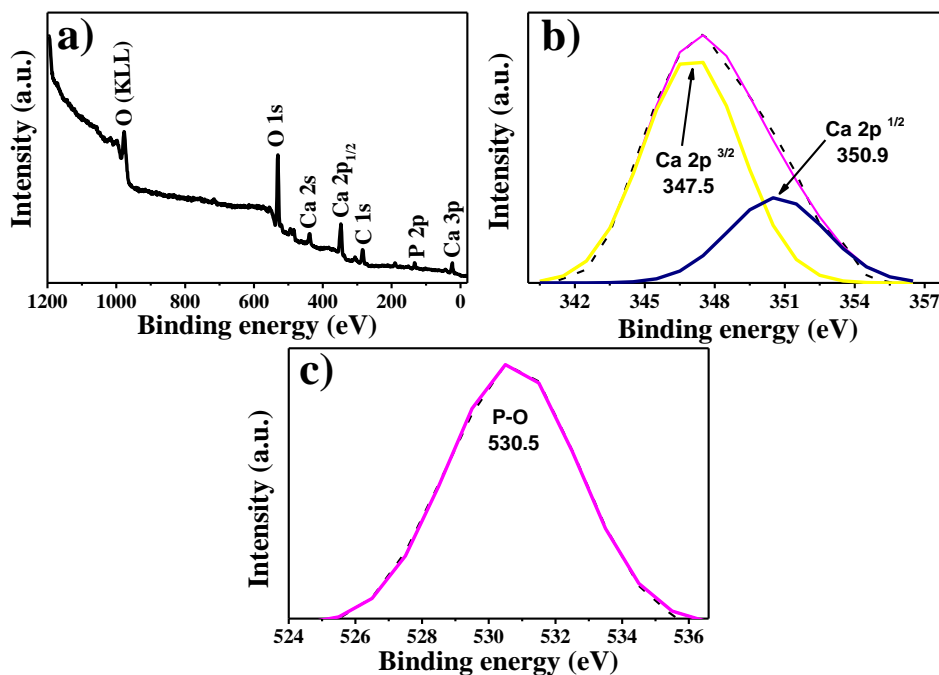


Figure 5. XPS spectrum: (a) general spectrum. High-resolution spectra of (b) Ca 2p and (c) O 1s.

#### 4. Conclusions

Reusing sea urchin spines (*Strongylocentrotus purpuratus*) for the synthesis of HA is a viable way to produce high-quality HA, which also contributes to the care of the environment. Biosynthesized material has the potential for use in the medical industry and other applications. The ideal biosynthesis temperature for the generation of high-purity HA using sea urchin spines was found to be between 500 and 700 °C—a lower temperature in relation to other works reported in the literature. The effect of temperature played an important role in the formation of the HA: as the temperature increased, the size of the crystals decreased, their resistance decreased and their purity or crystallinity decreased as well. This indicates that this research could be a starting point for the creation of HA on an industrial scale, by improving synthesis parameters. While this research proves that there are better parameters to be found by using different temperatures, there is still progress to be made in the production of HA while using lower biosynthesis energy.

**Author Contributions:** Conceptualization, P.A.L.M. and M.d.J.C.C.; methodology, N.S.G.V. and O.d.J.N.O.; software, A.R.V.N.; validation, C.M.G.G. and R.C.V.S.; formal analysis, C.M.G.G. and R.C.V.S.; investigation, N.S.G.V. and O.d.J.N.O.; resources, P.A.L.M. and A.R.V.N.; data curation, A.R.V.N.; writing—original draft preparation, N.S.G.V. and M.d.J.C.C.; writing—review and editing, R.C.V.S, P.A.L.M. and O.d.J.N.O.; visualization, C.M.G.G.; supervision, M.d.J.C.C. and P.A.L.M.; project administration, M.d.J.C.C. and P.A.L.M.; funding acquisition, CONACYT 4940. All authors have read and agreed to the published version of the manuscript.

**Funding:** The authors thank the support of CONACYT projects numbered 4940 and 295075.

**Acknowledgments:** The authors appreciate the support of the PRODEP with official number 511-6/2019-9670.

**Conflicts of Interest:** The authors declare no conflict of interest.

## References

- García-Garduño, M.V.; Reyes-Gasga, J. La Hidroxiapatita, Su Importancia En Los Tejidos Mineralizados Y Su Aplicación Biomédica. *TIP Rev. Espec. Cienc. Químico-Biológicas* **2006**, *9*, 90–95.
- Erdem, U.; Dogan, M.; Metin, A.U.; Baglar, S.; Turkoz, M.B.; Turk, M.; Nezir, S. Hydroxyapatite-Based Nanoparticles as a Coating Material for the Dentine Surface: An Antibacterial and Toxicological Effect. *Ceram. Int.* **2020**, *46*, 270–280. [[CrossRef](#)]
- Sorkhi, L.; Farrokhi-Rad, M.; Shahrabi, T. Electrophoretic Deposition of Hydroxyapatite–Chitosan–Titania on Stainless Steel 316 L. *Surfaces* **2019**, *2*, 458–467. [[CrossRef](#)]
- Lett, J.A.; Sagadevan, S.; Prabhakar, J.J.; Hamizi, N.A.; Badruddin, I.A.; Johan, M.R.; Marlinda, A.R.; Abdul Wahab, Y.; Khan, Y.; Mohammad, T. Drug Leaching Properties of Vancomycin Loaded Mesoporous Hydroxyapatite as Bone Substitutes. *Processes* **2019**, *7*, 826. [[CrossRef](#)]
- Li, T.-T.; Ling, L.; Lin, M.-C.; Jiang, Q.; Lin, Q.; Lin, J.-H.; Lou, C.-W. Properties and Mechanism of Hydroxyapatite Coating Prepared by Electrodeposition on a Braid for Biodegradable Bone Scaffolds. *Nanomaterials* **2019**, *9*, 679. [[CrossRef](#)] [[PubMed](#)]
- Witzler, M.; Ottensmeyer, P.F.; Gericke, M.; Heinze, T.; Tobiasch, E.; Schulze, M. Non-Cytotoxic Agarose/Hydroxyapatite Composite Scaffolds for Drug Release. *Int. J. Mol. Sci.* **2019**, *20*, 3565. [[CrossRef](#)]
- Sudhan, N.; Lavanya, N.; Leonardi, S.G.; Neri, G.; Sekar, C. Monitoring of Chemical Risk Factors for Sudden Infant Death Syndrome (SIDS) by Hydroxyapatite–Graphene–MWCNT Composite-Based Sensors. *Sensors* **2019**, *19*, 3437. [[CrossRef](#)]
- Ragab, A.; Ahmed, I.; Bader, D. The Removal of Brilliant Green Dye from Aqueous Solution Using Nano Hydroxyapatite/chitosan Composite as a Sorbent. *Molecules* **2019**, *24*, 847. [[CrossRef](#)]
- Gheysari, H.; Mohandes, F.; Mazaheri, M.; Dolatyar, B.; Askari, M.; Simchi, A. Extraction of Hydroxyapatite Nanostructures from Marine Wastes for the Fabrication of Biopolymer-Based Porous Scaffolds. *Mar. Drugs* **2020**, *18*, 26. [[CrossRef](#)]
- Venkatesan, J.; Lowe, B.; Manivasagan, P.; Kang, K.-H.; Chalisserry, E.P.; Anil, S.; Kim, D.G.; Kim, S.-K. Isolation and Characterization of Nano-Hydroxyapatite from Salmon Fish Bone. *Materials* **2015**, *8*, 5426–5439. [[CrossRef](#)]
- Liu, Y.; Gu, J.; Fan, D. Fabrication of High-Strength and Porous Hybrid Scaffolds Based on Nano-Hydroxyapatite and Human-Like Collagen for Bone Tissue Regeneration. *Polymers* **2020**, *12*, 61. [[CrossRef](#)] [[PubMed](#)]
- Salamanca, E.; Hsu, C.C.; Yao, W.L.; Choy, C.S.; Pan, Y.H.; Teng, N.-C.; Chang, W.-J. Porcine Collagen–Bone Composite Induced Osteoblast Differentiation and Bone Regeneration In Vitro and In Vivo. *Polymers* **2020**, *12*, 93. [[CrossRef](#)] [[PubMed](#)]
- Ofudje, E.A.; Rajendran, A.; Adeogun, A.I.; Idowu, M.A.; Kareem, S.O.; Pattanayak, D.K. Synthesis of Organic Derived Hydroxyapatite Scaffold from Pig Bone Waste for Tissue Engineering Applications. *Adv. Powder Technol.* **2018**, *29*, 1–8. [[CrossRef](#)]
- Rahavi, S.S.; Ghaderi, O.; Monshi, A.; Fathi, M.H. A Comparative Study on Physicochemical Properties of Hydroxyapatite Powders Derived from Natural and Synthetic Sources. *Russ. J. Non-Ferrous Met.* **2017**, *58*, 276–286. [[CrossRef](#)]
- Shi, P.; Liu, M.; Fan, F.; Yu, C.; Lu, W.; Du, M. Characterization of Natural Hydroxyapatite Originated from Fish Bone and Its Biocompatibility with Osteoblasts. *Mater. Sci. Eng. C* **2018**, *90*, 706–712. [[CrossRef](#)] [[PubMed](#)]
- Ferro, A.C.; Guedes, M. Mechanochemical Synthesis of Hydroxyapatite Using Cuttlefish Bone and Chicken Eggshell as Calcium Precursors. *Mater. Sci. Eng. C* **2019**, *97*, 124–140.
- Mancilla-Sanchez, E.; Gómez-Gutiérrez, C.M.; Guerra-Rivas, G.; Soto-Robles, C.A.; Vilchis-Nestor, A.R.; Vargas, E.; Luque, P.A. Obtaining Hydroxyapatite from the Exoskeleton and Spines of the Purple Sea Urchin *Strongylocentrotus Purpuratus*. *Int. J. Appl. Ceram. Technol.* **2019**, *16*, 438–443. [[CrossRef](#)]
- Balitaan, J.N.I.; Yeh, J.-M.; Santiago, K.S. Marine Waste to a Functional Biomaterial: Green Facile Synthesis of Modified- $\beta$ -Chitin from *Uroteuthis Duvauceli* Pens (*Gladius*). *Int. J. Biol. Macromol.* **2019**, *19*. [[CrossRef](#)]
- Hoshijima, U.; Hofmann, G.E. Variability of Seawater Chemistry in a Kelp Forest Environment Is Linked to in Situ Transgenerational Effects in the Purple Sea Urchin, *Strongylocentrotus Purpuratus*. *Front. Mar. Sci.* **2019**, *6*, 1–18. [[CrossRef](#)]
- Palleiro-Nayar, J.S.; Salgado-Rogel, M.L.; Aguilar-Montero, D. La Pesca de Erizo Morado, *Strongylocentrotus Purpuratus*, Y Su Incremento Poblacional En Baja California, México. *Cienc. Pesq* **2008**, *16*, 29–35.

21. Rey-Méndez, M.; Tourón, N.; Rodríguez-Castro, B.; Rama-Villar, A.; Fernández-Silva, I.; González, N.; Martínez, D.; Ojea, J.; Catoira, J.L. Growth and Improvement of the Gonadal Index in the Cultivation of the Sea Urchin *Paracentrotus Lividus* (Echinoida: Echinidae) in Galicia (Spain). *Rev. Biol. Trop.* **2015**, *63*, 261–272.
22. Andrew, N.L.; Agatsuma, Y.; Ballesteros, E.; Bazhin, A.G.; Creaser, E.P.; Barnes, D.K.A.; Botsford, L.W.; Bradbury, A.; Campbell, A.; Dixon, J.D. Status and Management of World Sea Urchin Fisheries. In *Oceanography and Marine Biology, an Annual Review*; CRC Press: Boca Raton, FL, USA, 2002; Volume 40, pp. 351–438.
23. Schneider, F.; Parsons, S.; Clift, S.; Stolte, A.; McManus, M.C. Collected Marine litter—A Growing Waste Challenge. *Mar. Pollut. Bull.* **2018**, *128*, 162–174. [[CrossRef](#)] [[PubMed](#)]
24. Michał, W.; Ewa, D.; Tomasz, C. Lecithin-Based Wet Chemical Precipitation of Hydroxyapatite Nanoparticles. *Colloid Polym. Sci.* **2015**, *293*, 1561–1568. [[CrossRef](#)] [[PubMed](#)]
25. Yu, H.-N.; Hsu, H.-C.; Wu, S.-C.; Hsu, C.-W.; Hsu, S.-K.; Ho, W.-F. Characterization of Nano-Scale Hydroxyapatite Coating Synthesized from Eggshells Through Hydrothermal Reaction on Commercially Pure Titanium. *Coatings* **2020**, *10*, 112. [[CrossRef](#)]
26. Namduri, H.; Nasrazadani, S. Quantitative Analysis of Iron Oxides Using Fourier Transform Infrared Spectrophotometry. *Corros. Sci.* **2008**, *50*, 2493–2497. [[CrossRef](#)]
27. Raizada, P.; Shandilya, P.; Singh, P.; Thakur, P. Solar Light-Facilitated Oxytetracycline Removal from the Aqueous Phase Utilizing a H<sub>2</sub>O<sub>2</sub>/ZnWO<sub>4</sub>/CaO Catalytic System. *J. Taibah Univ. Sci.* **2017**, *11*, 689–699. [[CrossRef](#)]
28. Vecchio, K.S.; Zhang, X.; Massie, J.B.; Wang, M.; Kim, C.W. Conversion of Sea Urchin Spines to Mg-Substituted Tricalcium Phosphate for Bone Implants. *Acta Biomater.* **2007**, *3*, 785–793. [[CrossRef](#)] [[PubMed](#)]
29. Shavandi, A.; Bekhit, A.E.-D.A.; Ali, A.; Sun, Z. Synthesis of Nano-Hydroxyapatite (nHA) from Waste Mussel Shells Using a Rapid Microwave Method. *Mater. Chem. Phys.* **2015**, *149*, 607–616. [[CrossRef](#)]
30. Sivakumar, M.; Kumar, T.S.S.; Shantha, K.L.; Rao, K.P. Development of Hydroxyapatite Derived from Indian Coral. *Biomaterials* **1996**, *17*, 1709–1714. [[CrossRef](#)]
31. Sabu, U.; Logesh, G.; Rashad, M.; Joy, A.; Balasubramanian, M. Microwave Assisted Synthesis of Biomorphic Hydroxyapatite. *Ceram. Int.* **2019**, *45*, 6718–6722. [[CrossRef](#)]
32. Pang, Y.X.; Bao, X. Influence of Temperature, Ripening Time and Calcination on the Morphology and Crystallinity of Hydroxyapatite Nanoparticles. *J. Eur. Ceram. Soc.* **2003**, *23*, 1697–1704. [[CrossRef](#)]
33. Sunil, B.R.; Jagannatham, M. Producing Hydroxyapatite from Fish Bones by Heat Treatment. *Mater. Lett.* **2016**, *185*, 411–414. [[CrossRef](#)]
34. Barakat, N.A.M.; Khil, M.S.; Omran, A.M.; Sheikh, F.A.; Kim, H.Y. Extraction of Pure Natural Hydroxyapatite from the Bovine Bones Bio Waste by Three Different Methods. *J. Mater. Process. Technol.* **2009**, *209*, 3408–3415. [[CrossRef](#)]
35. Pasteris, J.D.; Wopenka, B.; Freeman, J.J.; Rogers, K.; Valsami-Jones, E.; Van Der Houwen, J.A.M.; Silva, M.J. Lack of OH in Nanocrystalline Apatite as a Function of Degree of Atomic Order: Implications for Bone and Biomaterials. *Biomaterials* **2004**, *25*, 229–238. [[CrossRef](#)]
36. Rutherford, R.S.; Van Staden, J. Towards a Rapid near-Infrared Technique for Prediction of Resistance to Sugarcane borer *Eldana Saccharina Walker* (Lepidoptera: Pyralidae) Using Stalk Surface Wax. *J. Chem. Ecol.* **1996**, *22*, 681–694. [[CrossRef](#)]
37. Santos, C.; Turiel, S.; Gomes, P.S.; Costa, E.; Santos-Silva, A.; Quadros, P.; Duarte, J.; Battistuzzo, S.; Fernandes, M.H. Vascular Biosafety of Commercial Hydroxyapatite Particles: Discrepancy between Blood Compatibility Assays and Endothelial Cell Behavior. *J. Nanobiotechnol.* **2018**, *16*, 27. [[CrossRef](#)]
38. Ramesh, S.; Tan, C.Y.; Hamdi, M.; Sopyan, I.; Teng, W.D. The Influence of Ca/P Ratio on the Properties of Hydroxyapatite Bioceramics. In *International Conference on Smart Materials and Nanotechnology in Engineering*; International Society for Optics and Photonics: Harbin, China, 2007; Volume 6423, p. 64233A.
39. Guo, X.; Li, D. Synthesis of Hydroxyapatite Containing Some Trace Amounts Elements in Simulated Body Fluids. *Iran. J. Chem. Chem. Eng.* **2019**, *38*, 83–91.
40. Latocha, J.; Wojasiński, M.; Sobieszuk, P.; Gierlotka, S.; Ciach, T. Impact of Morphology-Influencing Factors in Lecithin-Based Hydroxyapatite Precipitation. *Ceram. Int.* **2019**, *45*, 21220–21227. [[CrossRef](#)]
41. Ungureanu, D.N.; Angelescu, N.; Ion, R.M.; Stoian, E.V.; Rizescu, C.Z. Synthesis and Characterization of Hydroxyapatite Nanopowders by Chemical Precipitation. *Recent Res. Commun. Autom. Signal Process. Nanotechnol. Astron. Nucl. Phys.* **2011**, *9*, 296–301.
42. Pyo, E.; Lee, K.; Jang, M.J.; Ko, I.; Kim, C.S.; Choi, S.M.; Lee, S.; Kwon, K. Cobalt Incorporated Hydroxyapatite Catalyst for Water Oxidation. *Chem. Cat. Chem.* **2019**, *11*, 5425–5429. [[CrossRef](#)]

43. Surmenev, R.A.; Surmeneva, M.A.; Grubova, I.Y.; Chernozem, R.V.; Krause, B.; Baumbach, T.; Loza, K.; Epple, M. RF Magnetron Sputtering of a Hydroxyapatite Target: A Comparison Study on Polytetrafluorethylene and Titanium Substrates. *Appl. Surf. Sci.* **2017**, *414*, 335–344. [[CrossRef](#)]
44. Anwar, A.; Kanwal, Q.; Akbar, S.; Munawar, A.; Durrani, A.; Farooq, M.H. Synthesis and Characterization of Pure and Nanosized Hydroxyapatite Bioceramics. *Nanotechnol. Rev.* **2017**, *6*, 149–157. [[CrossRef](#)]



© 2020 by the authors. Licensee MDPI, Basel, Switzerland. This article is an open access article distributed under the terms and conditions of the Creative Commons Attribution (CC BY) license (<http://creativecommons.org/licenses/by/4.0/>).